MRI Imaging of the Hemodynamic Vasculature of Neuroblastoma Predicts Response to Anti-angiogenic Treatment

Konstantinos Zormpas-Petridis[1], Neil P. Jerome[1,2,3], Matthew D. Blackledge[1], Fernando Carceller[4], Evon Poon[4], Matthew Clarke[5], Ciara M. McErlean[1], Giuseppe Barone[6], Alexander Koers[4], Sucheta J. Vaidya[4], Lynley V. Marshall[4], Andrew D.J. Pearson[4], Lucas Moreno[7], John Anderson[6,9], Neil Sebire[8,9], Kieran McHugh[10], Dow-Mu Koh[1], Yinyin Yuan[5], Louis Chesler[4], Simon P. Robinson[1] and Yann Jamin[1,*].

[1] Division of Radiotherapy and Imaging, The Institute of Cancer Research, London and The Royal Marsden NHS Trust, 15 Cotswold Rd. Belmont, Sutton, Surrey SM2 5NG, United Kingdom.

[2] Department of Circulation and Medical Imaging, Norwegian University of Science and Technology (NTNU), Trondheim, Norway

[3] Clinic of Radiology and Nuclear Medicine, St. Olavs Hospital, Trondheim, Norway

[4] Division of Clinical Studies, The Institute of Cancer Research, London and The Royal Marsden NHS Trust, 15 Cotswold Rd. Belmont, Sutton, Surrey SM2 5NG, United Kingdom.

[5] Division of Molecular Pathology, The Institute of Cancer Research, London and The Royal Marsden NHS Trust, 15 Cotswold Rd. Belmont, Sutton, Surrey SM2 5NG, United Kingdom.

[6] Department of Pediatric Oncology, Great Ormond Street Hospital for Children, London WC1N 3JH, United Kingdom

[7] Clinical Research Unit, Pediatric Oncology, Hematology and Stem Cell Transplant Department, Hospital Infantil Universitario Ninõ Jesús, Madrid, Spain.

[8] Department of Histopathology, Great Ormond Street Hospital for Children, London WC1N 3JH, United Kingdom

[9] UCL Great Ormond Street Institute of Child Health, London WC1N 1EH, UK

[10] Department of Radiology, Great Ormond Street Hospital for Children, London WC1N 3JH, United Kingdom

Corresponding author:
Dr Yann Jamin, Centre for Cancer Imaging, Division of Radiotherapy and Imaging, The Institute of Cancer Research, London, 15 Cotswold Rd. Belmont, Sutton, Surrey SM2 5NG, UK. Email: yann.jamin@icr.ac.uk

Research Article

Running title: MRI predicts response to VEGFR-targeted therapy in neuroblastoma.

Keywords: MRI, Neuroblastoma, MYCN, VEGF, Biomarkers

Financial support: Cancer Research UK and EPSRC to the Cancer Imaging Centre at ICR, in association with the MRC and Department of Health (England) (C1060/A10334 and C1060/A16464), NHS funding to the NIHR Biomedicine Research Centre and the Clinical Research Facility in Imaging, the NIHR GOSH Biomedical Research Centre, The Rosetrees Trust (KZP), Children with Cancer UK (E.P.). Cancer Research UK Programme Grant (C18339) (L.C.). L.M. was funded by the Oak Foundation to the Royal Marsden and by Instituto de Salud Carlos III through Rio Hortega CM12/00260 and Juan Rodes JR15/00041 contracts. J.A. is supported by the NIHR GOSH Biomedical Research Centre and GOSHCC research leadership award. YJ is a Children with Cancer UK Research Fellow.

Conflict of interest: The authors have no conflict of interest to disclose

Word count: 4990

Number of tables: 0

Number of figures: 7

Abstract

Childhood neuroblastoma is a hypervascular tumor of neural origin for which antiangiogenic drugs are currently being evaluated; however, predictive biomarkers of treatment response, crucial for successful delivery of precision therapeutics, are lacking. We describe a MRI-pathological cross-correlative approach using intrinsic susceptibility (IS-) and susceptibility contrast (SC-) MRI to non-invasively map the vascular phenotype in neuroblastoma Th-MYCN transgenic mice treated with the vascular endothelial growth factor receptor inhibitor cediranib. We showed that the transverse MRI relaxation rate R_2* (s^{-1}) and fractional blood volume *f*BV (%) were sensitive imaging biomarkers of hemorrhage and vascular density, respectively, and were also predictive biomarkers of response to cediranib. Comparison with MRI and pathology from patients with MYCN-amplified neuroblastoma confirmed the high degree to which the Th-MYCN model vascular phenotype recapitulated that of the clinical phenotype, thereby supporting further evaluation of IS- and SC-MRI in the clinic. This study reinforces the potential role of functional MRI in delivering precision medicine to children with neuroblastoma.

Significance

This study shows that functional MRI predicts response to vascular-targeted therapy in a genetically-engineered murine model of neuroblastoma.

Introduction

Neuroblastoma is a tumor of childhood that arises within the embryonic sympatho-adrenal lineage of the neural crest. Neuroblastoma in high-risk form is chemoresistant, and metastatic relapse still accounts for 13% of all cancer-related death in children. Amplification of the proto-oncogene *MYCN* is the commonest genomic aberrations and defines a subgroup of children at high-risk of developing uncontrollable refractory or relapsing disease despite aggressive multimodal therapy (1).

In neuroblastoma, a high vascular index is associated with increased disseminated disease, amplification of *MYCN*, unfavorable histology and overall poor prognosis (2). Increased microvascular proliferation and other specific vascular morphological patterns are associated with even poorer prognosis, highlighting the pivotal role of angiogenesis in determining the clinical behavior of neuroblastoma (3,4). The vascular endothelial growth factor (VEGF) family is a key regulator of angiogenesis in neuroblastoma and high VEGF expression at the time of diagnosis is associated with poor outcome (5). Numerous anti-angiogenic therapies are being evaluated in early phase pediatric clinical trials in children with solid tumors, including the anti-VEGF monoclonal antibody bevacizumab in combination with temozolomide (BEACON, NCT02308527), and the tyrosine kinase inhibitors regorafenib (NCT02085148) and pazopanib as a single agent (NCT01956669) or in combination with metronomic oral topotecan (TOPAZ), as well as the panVEGFR inhibitor cediranib currently being evaluated in children with metastatic alveolar soft part sarcoma (NCT00942877).

Magnetic resonance imaging (MRI) is becoming the preferred clinical imaging technique for the management of children with neuroblastoma because of its exquisite soft tissue contrast. MRI provides excellent anatomical information at diagnosis and follow up while sparing exposure to ionising radiation associated with computed tomography (CT) (6). Advanced functional MRI techniques can additionally be used to define quantitative imaging biomarkers that inform on biologically relevant structure-function relationships in tumors *in vivo*. Perfusion MRI (pMRI) methodologies such as dynamic contrast enhanced (DCE-) MRI using low molecular weight gadolinium chelates are often used to evaluate vascular response to VEGF signaling inhibitors in adult oncology clinical trials. However, these techniques suffer from marked measurement variability and are challenging to perform in young children (7,8). Arterial spin labeling (ASL-) MRI is an emerging and attractive contrast-free

approach for the evaluation of cerebral perfusion, yet many challenges need to be overcome before its utility to assess vascular perfusion in extra-cranial tumors can be evaluated. Two complementary magnetic susceptibility-based MRI approaches are being actively exploited to assess tumor vascular function and response. Tumor vasculature has been studied using *i)* intrinsic susceptibility (IS-) MRI, which measures the intrinsic transverse relaxation (R_2*) contrast produced by paramagnetic deoxyhemoglobin within tumor blood vessels, and *ii)* susceptibility contrast (SC-) MRI, which relies on the intravenous administration of ultrasmall superparamagnetic iron oxide (USPIO) particles. Distribution of USPIO particles within tumors causes regional increases in tumor R_2* (ΔR_2*), from which the fractional blood volume (*f*BV, %) can be derived (9,10). The long intravascular half-life of USPIO particles enables steady state acquisition and high-resolution mapping of regional variations in tumor perfusion. Both R_2* and *f*BV has been shown to be sensitive imaging biomarkers of response to vascular-targeted therapies *in vivo* in the preclinical setting (11-13).

Imaging biomarkers must undergo stringent validation before they can be deployed clinically (14). Early imaging biomarker development demands close imaging-pathology correlation, to understand the biological processes underpinning the imaging measurement, which can be meaningfully studied using animal models. The Th-*MYCN* genetically-engineered mouse (GEM) model of neuroblastoma has been shown to faithfully recapitulate the major genetic and patho-physiological features of the childhood disease (12,15). The primary abdominal tumors in the Th-*MYCN* mice present with multiple para- and intra- tumoral anatomical landmarks detectable by conventional MRI, which can be used to ensure the accurate registration between the functional MRI-derived parametric maps and histopathology crucial for the validation of imaging biomarkers. The GEM models of neuroblastoma thus represent an information-rich platform with which to evaluate promising therapeutic strategies and associated non-invasive imaging biomarkers.

In this study, we investigated the utility of SC- and IS-MRI to inform on the functional tumor vasculature, and its response to the potent pan-VEGFR inhibitor cediranib, in tumors arising in the Th-*MYCN* GEM model of neuroblastoma. We then compared the regional distribution of tumor *f*BV and R_2* with aligned whole-slide digitized pathology stained for vessel density and red blood cell (RBC) aggregation respectively, and validated, via hotspot mapping and spatial statistics, to determine whether the MRI biomarkers can robustly characterize the

vascular phenotype of neuroblastoma *in vivo*. We also demonstrate here that both baseline *f*BV and R_2* are predictive imaging biomarkers of tumor response to cediranib. The pathological attributes associated with the differential sensitivity to cediranib treatment in the Th-*MYCN* model are discussed and positioned against available clinical MRI findings of *MYCN*-amplified neuroblastoma, including our initial experience with IS-MRI.

Materials and Methods

Animals

All experiments were approved by The Institute of Cancer Research Animal Welfare and Ethical Review Body and performed in accordance with the UK Home Office Animals (Scientific Procedures) Act 1986, the United Kingdom National Cancer Research Institute guidelines for the welfare of animals in cancer research (16) and the ARRIVE (animal research: reporting in vivo experiments) guidelines (17).

Transgenic Th-*MYCN* mice were genotyped to detect the presence of the human *MYCN* transgene (18). The study was performed using both male and female hemizygous mice, which developed palpable tumors at 50–130 days with a 25% penetrance. Tumor development was monitored weekly by palpation by an experienced animal technician. Mice with palpable tumors were then enrolled (Day 0) and their tumor volume was subsequently monitored by MRI. A total of 68 mice were enrolled with a median tumor volume of 801±63 mm^3 (median ± 1 s.e.m., ranging from 143 to 2055 mm^3). Mice were housed in specific pathogen-free rooms in autoclaved, aseptic microisolator cages (maximum of 4 mice per cage).

Preclinical study design

Study 1. We first evaluated the sensitivity of MRI to cediranib-induced acute modulation of neuroblastoma vasculature. IS- and SC-MRI were performed prior to (*Day 0*) and 24 hours after treatment started (*Day 2*). Mice were treated on *Day 1* with 6 mg/kg of cediranib p.o. (obtained under material transfer agreement with AstraZeneca, n=10) or vehicle (n=8). One mouse was excluded due to failed remote contrast injection. The 24h imaging timepoint was chosen based on *i)* preliminary evidence that cediranib does not elicit any significant volume reduction at this timepoint in the highly chemosensitive Th-*MYCN* model (12) and *ii)* cediranib caused significant reductions in DCE-MRI parameters at this timepoint in the adult Phase I clinical trial (19).

Study 2. In an additional cohort (n=12) we further evaluated the effect of sustained daily treatment, with IS- and SC-MRI performed prior to, 24 hours and 7 days after daily treatment with 6 mg/kg cediranib. MRI data were not collected from 2 mice at the 24h timepoint.

Study 3. Guided by the results of Study 2, we subsequently acquired IS-MRI data from additional Th-*MYCN* mice (n=25) prior to daily treatment with cediranib for 7 days (bringing the total number of mice from which pre-treatment R_2* data was acquired to 37). The volumetric response to cediranib over 7 days treatment was monitored by T_2-weighted MRI only, and compared with that from mice treated daily with vehicle (n=12).

MRI

All MRI studies were performed on a 7T Bruker horizontal bore MicroImaging system (Bruker Instruments, Ettlingen, Germany) using a 3cm birdcage volume coil. Anesthesia was induced by an intraperitoneal 5ml/kg injection of a combination of fentanyl citrate (0.315mg/ml) plus fluanisone (10mg/ml) (Hypnorm, Janssen Pharmaceutical, Oxford, UK) and midazolam (5mg/ml) (Roche, Welwyn Garden City, UK) and water (1:1:2). A lateral tail vein was cannulated with a 27G butterfly catheter (Hospira) for remote administration of USPIO particles. Core temperature was maintained at ~37°C with warm air blown through the magnet bore.

For all the mice, anatomical T_2-weighted transverse images were acquired from twenty contiguous 1 mm-thick slices through the mouse abdomen, using a rapid acquisition with refocused echoes (RARE) sequence with 4 averages of 128 phase encoding steps over a 3×3 cm field of view, an echo time (TE) of 36 ms, a repetition time (TR) of 4.5 s and a RARE factor of 8. These images were used to determine tumor volumes, and for planning the subsequent functional MRI measurements, which included optimization of the local field homogeneity using FASTmap algorithm and the measurement of the baseline transverse relaxation rate R_2* (s^{-1}), which is sensitive to the concentration of paramagnetic species, principally deoxyhemoglobin. R_2* was quantified using a multiple gradient-recall echo (MGE) sequence with 8 averages, and an acquisition time of 3 min 20 s. Images were acquired using 8 echoes spaced 3 ms apart, an initial TE of 6 ms, a flip angle α=45° and a TR of 200 ms. A dose of 150 μmol Fe/kg of the USPIO particle preparation P904 (overall

particle size ~25–30 nm diameter, Guerbet) was then administered intravenously. After 3 minutes to allow for equilibration, a second set of identical MGRE images acquired.

All the MRI data were acquired with a matrix size of 128x128 over a 3×3 cm field of view. Tumor volumes were determined using segmentation from regions of interest drawn on T_2-weighted images for each tumor-containing slice using OsiriX. Tumor R_2* maps were calculated from regions of interest drawn for each tumor-containing slice from the MGRE images acquired prior to and following administration of USPIO particles by fitting a single exponential to the signal intensity echo time curve on a voxel-by-voxel basis using a robust Bayesian approach using in-house software (ImageView, developed in IDL, ITT Visual Information Systems, Boulder, Colorado, USA). Parametric maps of tumor fBV (%) were subsequently calculated using the USPIO-induced change in R_2* (ΔR_2*), as described previously (20).

Tissue preparation for histology

Guided by T_2-weighted anatomical images, tumors were carefully excised and orientated for subsequent histopathological processing. Formalin-fixed and paraffin embedded tumors were cut in 3μm sections and were stained with hematoxylin and eosin (H&E) and for the murine vascular endothelial marker endomucin (rabbit EP3095, Millipore, Watford, UK). Whole-Slide images were digitized using a Hamamatsu NanoZoomer XR scanner (20x magnification, 0.46μm resolution, Hamamatsu, Japan).

MRI-histology alignment

The MRI slice of interest were visually aligned with digitized whole-slide H&E stained images using anatomical landmarks from T_2-weighted images, including, the shape of the tumor, the position of the kidneys, the position and/or orientation of tumor-displaced and –circumferentially surrounded abdominal aorta and renal aorta/vein and the presence of lymph nodes.

Computational pathology

Both red blood cells (RBC) and endomucin staining were automatically extracted from T_2-weighted MRI corresponding digitized whole-slide histopathological images for the validation of R_2* and *f*BV as biomarker of red blood cells aggregation and vascular perfusion. Histological images (0.46x0.46μm pixel resolution) were first split into tiles of 2000x2000 pixels (jpeg) for computational efficiency.

RBC extraction from HE-stained sections. A macro was written in Fiji to extract RBC from each tile by applying color deconvolution to extract the eosin color channel followed by the application of Otsu's automatic threshold detection method, both using ImageJ/Fiji plugins (with Java 8) (21). Algorithm accuracy was tested using independent annotation of 561 RBC and 591 non-RBC points in 9 samples.

Endomucin extraction from endomucin-stained IHC sections. A macro was written in Fiji to extract endomucin from each tile by applying color deconvolution to extract the brown color channel followed by the application of Maximum Entropy threshold detection method, both using ImageJ/Fiji plugins (Java 8). Algorithm accuracy was tested using independent annotation of stained/non-stained points (688/734) on 9 different samples.

Generation of RBC and endomucin parametric maps. Whole-slide images of RBC and endomucin staining were converted into binary and processed to match MRI resolution (234x234μm), with the fraction of pixels occupied by RBC or endomucin staining within 518x518 pixel-regions representing a single pixel in the final RBC map.

Comparison of R2 vs RBC and fBV vs endomucin parametric maps* was performed visually following the application the kernel density estimation (KDE) to display hotspots of high, above the 85th percentile for each tumor sample, R_2* and RBC (%), fBV (%) and endomucin staining (%) values using the 'MASS' package in R (22,23).

MRI-histology registration

Coherent point drift (CPD) registration algorithm. Accurate registration between histology and MRI images is essential to derive robust conclusions and apply spatial statistics. We applied the automatic CPD algorithm for both *i)* rigid and *ii)* non-rigid registration to corresponding pairs of images (R_2* or *f*BV maps and computed maps of red blood cells (RBC) and endomucin respectively) in Matlab (24). This algorithm was primarily selected because it preserves topological structures due to the coherent motion of the point sets. To avoid any bias, the point sets (features) from each map were edges extracted using a simple Canny edge detector. Indepedently, we also performed *iii)* a manual registration by rotation and scaling to match.

Statistical analysis

Statistical analysis was performed with GraphPad Prism 6 (GraphPad Software Inc., La Jolla, USA). The mean of median values for all the quantitative MRI parameters, the mean values for tumor volume, RBC and endomucin were used for statistical analysis with a 5% level of significance. Any significant differences in tumor volume and quantitative histopathological parameters were identified using Student's 2-tailed unpaired t-test, with a 5% level of significance. Significant correlations between the mean values. All linear correlations were determined by Pearson's correlation method. Level of significance was 5%.

Spatial statistics. The Mantel test, a non-parametric analysis of associations between corresponding positions of two distance matrices, was perfomed on registered pairs of MRI maps and computed maps of histopathological features using the "ade4" libray in R. Distance matrices were calculated using the "dist" function.

Clinical investigations

Based on the results of the preclinical investigations we aimed to i) evaluate the clinical relevance of the vascular phenotype observed in the Th-MYCN tumors by reviewing available diagnostic MRI data from patients with *MYCN*-amplified neuroblastoma, and ii) evaluate the feasibility of acquiring IS-MRI in children with neuroblastoma.

Informed consent was obtained from all parents or patients following IRB approval of the prospective study with IS-MRI at the Royal Marsden Hospital. For the retrospective review of routine diagnostic imaging at Great Ormond Street Hospital, anonymised data was provided to the researchers.

Retrospective analysis of MRI scans performed at initial diagnosis. Patients (n=19, 13 male/ 6 female) with confirmed *MYCN*-amplified disease included in this retrospective analysis were 1 day to 3.6 years old and imaged between May 2008 and July 2017 at Great Ormond Street Hospital. Exclusion criteria were *i)* no MRI at diagnosis or *ii)* MRI performed externally. Diagnostic imaging was performed on a 1.5 T Magnetom Avanto system (Siemens Healthcare, Erlangen, Germany) and included short time inversion recovery (STIR) T_2-weighted sequences (TE=60ms, TR=8000ms) and spectral attenuated inversion recovery (SPAIR) T_1-weighted BLADE sequence (TE=20ms, TR=600ms), prior and after the injection of Gd chelate based contrast agent, diffusion-weighted MRI sequence (TE=90ms, TR=2700ms, 5 b-values, b=0, 50-800s/mm^2). Slice thickness was 6mm and the field of view was adapted to each patient.

Prospective study of the feasibility of IS-MRI in patients with refractory/relapsing neuroblastoma. The 3 patients (n= 2 male/ 1 female) with refractory/relapsing disease included in this study were 5 to 7 years old and scanned between July 2013 and March 2015. MRI was performed on a 1.5 T Magnetom Avanto system using a phased-array body coil and included T_2-weighted sequence (turbo spin echo sequence TE=80ms, TR=7000ms) and T_1-weighted (TE=3ms, TR=10000ms) prior and after (last scan of the session) the injection of Gd chelate based contrast agent, and a Diffusion-weighted MRI sequence (TE=70ms, TR=3400ms, 6 b-values, b=0, 50-800s/mm^2). IS-MRI was performed in 2.5 min using a 2D multiple gradient-recall echo sequence (initial TE 5ms, 5 echoes, 10 ms apart, TR= 102 ms, flip angle= 40º). Images were analysed and R_2* quantified in Matlab.

Results

Baseline tumor fBV predicts response to cediranib in the Th-MYCN GEM model of neuroblastoma.

We first assessed changes in vascular function in Th-*MYCN* mice following treatment with cediranib. At the time of enrolment, the mean tumor *f*BV quantified using SC-MRI in the Th-*MYCN* mice (n=19) was 19.6±1%, consistent with the high vascular index of neuroblastoma. Treatment with cediranib caused an acute and highly significant reduction at 24 hours in tumor *f*BV ($\Delta fBV_{cediranib\_24h}$= -28±4% vs $\Delta fBV_{vehicle\_24h}$= -6±8%, p=0.0008), which was accompanied by a highly significant cytolentic response ($\Delta Volume_{cediranib\_D0\text{-}D2}$= 18±8% vs $\Delta Volume_{vehicle\_D0\text{-}D2}$= 53±11%, p=0.0006, Fig 1. A-F). Sustained daily treatment over 7 days caused a further significant reduction in *f*BV and anti-tumor activity (Fig 1. G-I). The average baseline *f*BV strongly correlated with the cediranib-induced reduction in *f*BV (r= -0.83, p=0.0008: Fig 1.J), and the value of *f*BV at baseline correlated with the subsequent cediranib-induced tumor volumetric response at day 7 (r= -0.65, p=0.02; Fig 1.K).

Baseline tumor R_2 predicts response to cediranib in the Th-MYCN GEM model of neuroblastoma.*

The analysis of the cohort of mice in which IS-MRI was routinely performed pre-treatment confirmed that cediranib effectively suppress of the aggressive tumor growth that is typical of this model ($\Delta Volume_{cediranib\_D0\text{-}D7}$= -16±5% vs $\Delta Volume_{vehicle\_D0\text{-}D7}$= 142±11%, p<0.0001, n=37 and n=12). However, a range of volumetric response, from progressive disease to partial response, was observed (Fig 2.A). Examination of our pre-treatment T_2-weighted anatomical images and native R_2* parametric maps revealed that responsive tumors exhibited a characteristically heterogeneous appearance, with areas of hypointense T_2 signal and relatively fast R_2* (R_2*= 113±4s^{-1}) (Fig 2.B&C), whereas progressive tumors typically demonstrated a more homogeneous, isointense appearance on T_2 and significantly slower native R_2* values (R_2*= 68±5s^{-1}, p<0.0001). Cediranib-induced changes in tumor volume over 7 days treatment correlated with native tumor R_2* measured before treatment (r= -0.72, p<0.0001, Fig 2.D).

Spatial heterogeneity in fBV reflects regional variations in the microvasculature of neuroblastoma.

The numerous anatomical landmarks (kidney, spleen, abdominal arteries, lymph nodes) clearly evident on T_2-weighted MRI were used to guide the careful excision and subsequent orientation of digitized pathology with SC- and IS-MRI-derived parametric maps. Intra-tumoral regional differences in *f*BV visually reflected spatial variations in computed maps of vascular endothelial endomucin staining, automatically extracted from high-resolution IHC images with an accuracy of 97%, after automatic registration using the coherent point drift (CPD) algorithm (Fig 3). This was corroborated by the location, size, shape and orientation of hotspots identified on kernel density estimation (KDE) maps of high values (above the 85^{th} percentile of each tumor sample) of *f*BV and endomucin (Fig 4. A). Application of the Mantel statistical test revealed significant ($p<0.05$) correlation ($0.10 < r < 0.58$, supplementary table 1) between the distance matrices of *f*BV and endomucin in 16 out of 23 tumors. Endomucin staining fraction corroborated the decrease in *f*BV measured longitudinally over 7 days, with significantly lower tumor values determined in the cohort treated with cediranib for 7 days than in the cohort of animals treated with a single dose of cediranib; both cohorts demonstrated lower values of *f*BV compared with the vehicle control group (Fig 4. B&C). Calculated tumor median values of *f*BV strongly correlated with median values of endomucin fraction area across the cohorts ($r= 0.85$, $p<0.0001$) (Fig 4.D).

Regional heterogeneity in R_2 reflects variations in RBC distribution in neuroblastoma*

Regional differences in parametric R_2* maps visually reflected spatial variations in extravasated RBC aggregation or RBC-filled necrotic areas (defined as large areas of cell damage) in the digitized maps, which was corroborated by the location, size, shape and orientation of hotspots on KDE maps of high values (above the 85^{th} percentile of each tumor sample) of R_2* and RBC, automatically extracted from high-resolution H&E-stained images with an accuracy of 99.7%, after automatic registration using the CPD algorithm (Fig 5). The Mantel statistical test revealed significant ($p<0.05$) spatial correlation ($0.10 < r < 0.76$, Supplementary table 2) between the distance matrices of R_2* and RBC in 9 out of 12 tumors. Calculated tumor median values of R_2* strongly correlated with the mean values of RBC fraction area ($r=0.87$, $p<0.0003$). Tumor median R_2* and mean value of RBC fraction also correlated with endomucin staining ($r = 0.53$, $p = 0.08$ and $r = 0.64$, $p = 0.02$, respectively).

Innate resistance to cediranib is associated with a differentiating phenotype

We then performed a semi-quantitative analysis to calibrate the tumor R_2* phenotype against pathological evaluation of aligned H&E stained sections (Fig 6, Supplementary table 3). For tumors with a median R_2* between ~80 and ~110s^{-1}, increasing tumor median R_2* reflected increasing area/proportion of the tumor presenting with a hemorrhagic and hypervascular phenotype, characterized by large sinusoidal-shaped vessels. In comparison, non-hemorrhagic regions remained well-vascularized but with markedly reduced hemorrhage and smaller capillary-like shape vessels. In these tumors, the extravasated RBCs conserved their biconcave shape and appeared intact. Tumors with a median R_2*>110s^{-1} additionally presented with large necrotic regions filled with both intact and damaged RBCs. Tumors exhibiting a median R_2* < 70s^{-1}, (comparable to tumors which progressed while on cediranib), presented a very different phenotype, characterized by the absence of hemorrhage (including in necrotic areas), reduced microvessel density with smaller more regular capillaries-like vessels, and large regions of differentiating neuroblasts (yet with only very few mature ganglion cells) arranged in islands, separated by a large amount of neuropil.

MYCN-amplified childhood neuroblastomas are hemorrhagic

To understand the relevance of the tumor MRI phenotypes observed in the Th-*MYCN* GEM mouse to *MYCN*-driven childhood neuroblastoma, we reviewed anatomical T_2-weighted, T_1-weighted and contrast enhanced (CE-) T_1-weighted images, as well as diffusion-weighted (DW-) MRI-derived apparent diffusion coefficient (ADC) maps, acquired from 19 patients with *MYCN*-amplified neuroblastoma at the time of diagnosis. All patients presented with abdominal tumors showing a high degree of heterogeneity (both hyper- and hypo-intensity) on T_2-weighted MRI and regional hyper-intensity on T_1-weighted MRI (Figure 7.A-E). Based on the well-established appearance of ageing blood on both T_2- and T_1-weighted MRI in hematoma (Figure 7.F), this appearance suggests the presence of blood products at different stage of hemoglobin degradation. Most tumors presented a central region which did not enhance on CE-MRI and showed elevated ADC values, suggesting the presence of large areas of non-viable tissue. Additionally, a few tumors presented with cystic components, with/without blood. Interestingly, 5 out of the 19 patients also presented with contiguous or satellite masses showing homogeneous signal on both T_1 (isointense) and T_2 (hyperintense) MRI, homogeneous contrast enhancement and low ADC values, indicative of water

restriction (Figure 7.B and C). This MRI phenotype suggests a non-hemorrhagic and cellular-dense tumor phenotype within these lobes.

We also compared the radiology of two cases of ganglioneuroblastoma: a ganglioneuroblastoma intermixed (GNB) and ganglioneuroblastoma nodular (GNBn), two entitites that are uncommonly MYCN-amplified. Yet GNB nodular are characterized by the presence of macroscopic undifferentiated neuroblastoma nodule(s) of Schwannian stroma-poor components coexisting with ganglioneuroblastoma-intermixed of stroma- rich component or ganglioneuroma (fully differentiated) of stroma-dominant component. The neuroblastoma nodule in the GNBn was easily identifiable with low ADC values, consistent with a stroma-poor neuroblastoma phenotype, and demonstrated marked hypointensity on T_2-weighted images, hyper-intensity on T_1-weighted images and high gadolinium avidity, overall suggesting that the neuroblastic nodule presented a highly vascular and hemorrhagic phenotype.

Initial experience with IS-MRI in children with neuroblastoma

Based on the initial results obtained in the Th-*MYCN* model, we have introduced IS-MRI into clinical trials in patients with relapsed/refractory neuroblastoma as a proof of concept. Our initial experience based on three patients scanned at 1.5T (Figure 7.G) showed that tumors (n=5) presented with a heterogeneous regional distribution of R_2*, with tumor median R_2* values ranging from 20 to 41s^{-1} (Figure 7.H), a range similar to the one measured in mice when corrected for the difference of magnetic field strength. Regionally, higher R_2* values were associated with hypo-intensity on T_2-weighted images, higher gadolinium avidity and lower ADC values. Combined with the apparent hemorrhagic nature of MYCN-amplified neuroblastoma, this pilot study suggests that IS-MRI should be prospectively evaluated in children with neuroblastoma to determine its clinical utility as an imaging biomarker.

Discussion

There is a current paradigm shift toward a stratified precision medicine approach for children with cancer. Central to this approach is the integration of both genomic and biological information including pharmacodynamic and predictive biomarkers of response to incorporate urgently-needed novel therapies into treatment schedules. With increasing evidence for the contribution of angiogenesis in determining and predicting the biological behavior of neuroblastoma, therapeutic approaches targeting the unique vascular phenotype of neuroblastoma are being accelerated in early phase pediatric clinical trials. However, there are currently no validated biomarkers predicting the clinical response or therapeutic benefits to anti-angiogenic therapy.

Whilst MRI is becoming the preferred clinical imaging method in the management of children with neuroblastoma particularly at diagnosis and for routine follow-up, the unique ability of advanced functional MRI techniques to non-invasively quantify changes in tumor vascular architecture and function has not yet been fully exploited (25). In this study, we have utilized the multiple intra- and para- anatomical tumor landmarks detectable on conventional T_2-weighted MRI in the Th-*MYCN* mouse, together with the CDP algorithm for registration to develop a robust MRI-histopathology correlation pipeline. The use of KDE hotspot mapping and non-parametric Mantel statistical test demonstrated that *f*BV, measured *in vivo* by SC-MRI, spatially correlates with stained area for the endothelial cell marker endomucin in tumors arising in the Th-*MYCN* mouse model of neuroblastoma. This approach thus validates *f*BV as a sensitive and but also a specific imaging biomarker of tumor vascular perfusion, and its therapeutic modulation by the potent VEGFR inhibitor cediranib. Furthermore, we found a negative correlation between tumor *f*BV and cediranib-mediated changes in *f*BV, suggesting baseline *f*BV as a potential predictive biomarker of vascular response to VEGFR inhibition. Importantly, our data suggest that both baseline tumor *f*BV and R_2* are predictive of the longer-term tumor response to VEGFR-targeted therapies such as cediranib.

Several pre-clinical studies have demonstrated that quantitation of tumor fBV using SC-MRI provides a sensitive biomarker of response to vascular-targeted agents *in vivo* (10,11,13). The data herein highlights the potential of SC-MRI to assess neuroblastoma vascular response to VEGF signaling inhibitors (26-29), and to MYCN-targeted therapeutics whose mechanism of

action is predicted to elicit an anti-angiogenic effect (30-33). For example, direct silencing of *MYCN* through bromodomain extra terminal (BET) domain inhibition, destabilization of MYCN protein via the selective targeting of Aurora A kinase or mTOR/PI3k signaling, and inhibition of anaplastic lymphoma kinase (ALK) and RET kinases (reviewed in (34)) have all been linked with angiogenic blockade in aligned preclinical trials against neuroblastoma or other pediatric solid tumors (31,32,35-37).

The high vascular permeability and density present in the Th-*MYCN* tumors and detected by IS- and SC-MRI illustrate the archetypal VEGF-driven vascular remodeling triggered by members of the *MYC* family oncogenes (31,38). There is increasing evidence that enhanced angiogenic signaling is part of a wider *MYC*-driven adaptive program to nutrient deprivation, to which *MYC*-driven tumors rapidly develop an addiction to maintain their growth (38,39). As a result, any blockade of this program via *MYC* deactivation, metabolic inhibition or vascular blockade triggers a wave of apoptosis, resulting in the unique rapid tumor debulking observed in MYC-driven tumors (38,39). The correlation between baseline *f*BV and R_2* and cediranib-induced tumor debulking established in this study illustrates a similar dependence on *MYCN*-driven angiogenic and vascular remodeling in the Th-*MYCN* GEM model. In contrast, tumors at the lower range of baseline R_2* and *f*BV values, which progress despite cediranib treatment, presented with a more normalized vasculature. We also identified tumors with large areas of differentiating neuroblasts, a phenotype similar to that in *MYCN*-driven GEM models of neuroblastoma harboring constitutive activation of *ALK*, and in which reduced VEGFR signaling has been reported (30,40,41). Clinically, differentiated neuroblastoma displays low vascularity (2,3), partly due to the release strong anti-angiogenic factors which directly antagonize the effect of VEGF (42,43). Additionally, in differentiating, schwannian-stroma poor neuroblastoma, VEGF-mediated cross talk between differentiating neuroblasts and endothelial cells has been identified which mimics normal vascular maturation in the developing nervous system (44). Overall in this study, reduced tumor sensitivity to cediranib was associated with a more stable vascular phenotype, suggesting a reduced dependence of these non-responsive tumors on VEGF signaling to sustain growth.

Genetically-engineered models of cancer have been shown to faithfully recapitulate the major molecular and histopathological features of human cancer, and to have a strong predictive power for clinical drug response and resistance (45). Neuroblastoma, and pediatric cancers in general, are particularly amenable for genetically modelling as they are only driven by a few genetic aberrations. Tumors arising in the Th-*MYCN* mouse model of neuroblastoma are

stroma-poor, undifferentiated or poorly differentiated with a high mitosis-karyorrhexis index, closely resembling the histology of *MYCN*-amplified tumors in the >18-month age group (15). The high tumor *f*BV values of ~20% reported here are consistent with the unique hypervascular phenotype of childhood neuroblastoma. The median endomucin staining area in the Th-*MYCN* tumors (2.3%) is consistent with the mean stained area of endothelial cell marker CD31 (1.7%) in a cohort of 458 primary childhood neuroblastomas (4). Structurally, the large areas of irregular sinusoidal vessels found in the hemorrhagic regions of Th-*MYCN* tumors emulate the major unstable vascular patterns associated with unfavorable clinical prognosis. In contrast, tumors with lower R_2*, differentiated or not, presented a more normalized vascular pattern associated with favorable prognosis factors in primary neuroblastoma. Our retrospective radiological analysis of 19 cases of *MYCN*-amplified neuroblastoma revealed that all tumors presented with a MRI phenotype consistent with hemorrhage. Additionally, our initial experience with IS-MRI in children with refractory/relapse neuroblastoma demonstrated a range of tumor median R_2* values, comparable to those measured in the Th-*MYCN* model when corrected for the difference in magnetic field strength (46). Collectively these data demonstrate that the Th-*MYCN* GEM model of neuroblastoma recapitulates the pathophysiology of childhood neuroblastoma and provides a unique clinically-relevant and information-rich platform to identify and validate imaging biomarkers of the neuroblastoma microenvironment.

DCE-MRI and CT-based functional imaging are commonly used to evaluate tumor perfusion in the clinic. Yet their associated biomarkers are difficult to interpret as they reflect both vascular perfusion and permeability. More importantly, the acquisition of robust DCE-MRI data can be challenging in young children (7) and CT-based functional imaging methodologies should be preferentially avoided due to the higher inherent sensitivity of children to the negative effects of ionizing radiation (6). The data herein provide a strong rationale for the incorporation of both IS- and SC-MRI into functional imaging-embedded clinical trials for new therapeutic strategies that directly or indirectly modulate neuroblastoma vascular phenotype. IS-MRI is a rapid, quantitative, safe and non-invasive R_2* relaxometry measurement that has become the reference measurement to assess both liver and cardiac iron content and a primary endpoint in pediatric clinical trials in highly-transfused children suffering from hematological diseases who are at risk of liver and cardiac iron overload (47). The multi-gradient recalled echo MRI sequence is universally available on clinical MRI scanners and IS-MRI can be easily incorporated in the neuroblastoma clinic, as demonstrated

herein, adding only two and half minutes to the current routine scanning session. IS-MRI has been incorporated in a ancillary functional imaging study of the BEACON Neuroblastoma trial. This study also demonstrates that hemorrhage detectable with IS-MRI, or the absence thereof, could hold prognostic/diagnostic value. Clinically, the hemorrhagic nature of undifferentiated neuroblastoma is well described, yet its routine reporting remains only anecdotal (48). Its value for risk-stratification could be explored by introducing non-invasive IS-MRI at the time of diagnosis. As a matter of fact, introducing susceptibility-weighted imaging (SW-MRI), a variant of IS-MRI, which combines the information from both the magnitude and the phase of the MR signal, would quantify hemorrhage with the added value of detecting calcification (opposite phase to hemorrhage). SW-MRI can assist in the differential diagnosis of neuroblastoma (frequently calcified) versus Wilms' tumors (seldom calcified) as this not easily detected on conventional MRI. SC-MRI, which combines R_2* mapping with the use of USPIO particles, does not require bolus timing or complex image acquisition schemes, and provides an attractive steady-state imaging alternative to DCE-MRI. Recent clinical studies highlighting the safe off-label use of the USPIO preparation ferumoxytol for MRI in adults and children is a promising step-forward, warranting further evaluation of the approach in clinical trials (49).

In summary, the robust MRI-pathology cross-validation methodology used in this study validates IS- and SC- MRI as robust non-invasive imaging techniques to characterize, quantify and map the unique vascular phenotype of neuroblastoma and its therapeutic modulation. With the central role of angiogenesis in determining and predicting the clinical behavior of neuroblastoma, baseline *f*BV and R_2*, have the potential to provide diagnostics and prognosis information at the time of diagnosis and provide currently unavailable predictive and pharmacodynamic biomarkers for anti-angiogenic therapy against neuroblastoma. Lastly, this study highlights the potential role of functional MRI in delivering precision medicine to children with neuroblastoma.

Acknowledgments: AstraZeneca for the supply of cediranib.

References

1. Matthay KK, Maris JM, Schleiermacher G, Nakagawara A, Mackall CL, Diller L*, et al.* Neuroblastoma. Nat Rev Dis Primers **2016**;2:16078
2. Meitar D, Crawford SE, Rademaker AW, Cohn SL. Tumor angiogenesis correlates with metastatic disease, N-myc amplification, and poor outcome in human neuroblastoma. J Clin Oncol **1996**;14:405-14
3. Peddinti R, Zeine R, Luca D, Seshadri R, Chlenski A, Cole K*, et al.* Prominent microvascular proliferation in clinically aggressive neuroblastoma. Clin Cancer Res **2007**;13:3499-506
4. Tadeo I, Bueno G, Berbegall AP, Fernandez-Carrobles MM, Castel V, Garcia-Rojo M*, et al.* Vascular patterns provide therapeutic targets in aggressive neuroblastic tumors. Oncotarget **2016**;7:19935-47
5. Jakovljevic G, Culic S, Stepan J, Bonevski A, Seiwerth S. Vascular endothelial growth factor in children with neuroblastoma: a retrospective analysis. J Exp Clin Cancer Res **2009**;28:143
6. Brisse HJ, McCarville MB, Granata C, Krug KB, Wootton-Gorges SL, Kanegawa K*, et al.* Guidelines for imaging and staging of neuroblastic tumors: consensus report from the International Neuroblastoma Risk Group Project. Radiology **2011**;261:243-57
7. Miyazaki K, Jerome NP, Collins DJ, Orton MR, d'Arcy JA, Wallace T*, et al.* Demonstration of the reproducibility of free-breathing diffusion-weighted MRI and dynamic contrast enhanced MRI in children with solid tumours: a pilot study. Eur Radiol **2015**;25:2641-50
8. O'Connor JP, Jayson GC. Do imaging biomarkers relate to outcome in patients treated with VEGF inhibitors? Clin Cancer Res **2012**;18:6588-98
9. Wu EX, Tang H, Jensen JH. Applications of ultrasmall superparamagnetic iron oxide contrast agents in the MR study of animal models. NMR Biomed **2004**;17:478-83
10. Robinson SP, Howe FA, Griffiths JR, Ryan AJ, Waterton JC. Susceptibility contrast magnetic resonance imaging determination of fractional tumor blood volume: a noninvasive imaging biomarker of response to the vascular disrupting agent ZD6126. Int J Radiat Oncol Biol Phys **2007**;69:872-9
11. Robinson SP, Boult JKR, Vasudev NS, Reynolds AR. Monitoring the Vascular Response and Resistance to Sunitinib in Renal Cell Carcinoma In Vivo with Susceptibility Contrast MRI. Cancer Res **2017**;77:4127-34
12. Jamin Y, Tucker ER, Poon E, Popov S, Vaughan L, Boult JK*, et al.* Evaluation of clinically translatable MR imaging biomarkers of therapeutic response in the TH-MYCN transgenic mouse model of neuroblastoma. Radiology **2013**;266:130-40
13. Vlachogiannis G, Hedayat S, Vatsiou A, Jamin Y, Fernandez-Mateos J, Khan K*, et al.* Patient-derived organoids model treatment response of metastatic gastrointestinal cancers. Science **2018**;359:920-6
14. O'Connor JP, Aboagye EO, Adams JE, Aerts HJ, Barrington SF, Beer AJ*, et al.* Imaging biomarker roadmap for cancer studies. Nat Rev Clin Oncol **2017**;14:169-86

15. Moore HC, Wood KM, Jackson MS, Lastowska MA, Hall D, Imrie H, *et al.* Histological profile of tumours from MYCN transgenic mice. J Clin Pathol **2008**;61:1098-103
16. Workman P, Aboagye EO, Balkwill F, Balmain A, Bruder G, Chaplin DJ, *et al.* Guidelines for the welfare and use of animals in cancer research. Br J Cancer **2010**;102:1555-77
17. Kilkenny C, Browne WJ, Cuthill IC, Emerson M, Altman DG. Improving bioscience research reporting: the ARRIVE guidelines for reporting animal research. PLoS Biol **2010**;8:e1000412
18. Weiss WA, Aldape K, Mohapatra G, Feuerstein BG, Bishop JM. Targeted expression of MYCN causes neuroblastoma in transgenic mice. The EMBO journal **1997**;16:2985-95
19. Drevs J, Siegert P, Medinger M, Mross K, Strecker R, Zirrgiebel U, *et al.* Phase I clinical study of AZD2171, an oral vascular endothelial growth factor signaling inhibitor, in patients with advanced solid tumors. J Clin Oncol **2007**;25:3045-54
20. Tropres I, Lamalle L, Peoc'h M, Farion R, Usson Y, Decorps M, *et al.* In vivo assessment of tumoral angiogenesis. Magn Reson Med **2004**;51:533-41
21. Otsu N. A Threshold Selection Method from Gray-Level Histograms. IEEE Transactions on Systems, Man and Cybernetics **1979**;9:62-6
22. Parzen E. On Estimation of a Probability Density Function and Mode. Ann Math Statist **1962**;33:1065-76
23. Chainey S, Tompson L, Uhlig S. The Utility of Hotspot Mapping for Predicting Spatial Patterns of Crime. Security Journal **2008**;21:4-28
24. Myronenko A, Song XB. Point Set Registration: Coherent Point Drift. Ieee T Pattern Anal **2010**;32:2262-75
25. Manias KA, Gill SK, MacPherson L, Foster K, Oates A, Peet AC. Magnetic resonance imaging based functional imaging in paediatric oncology. Eur J Cancer **2017**;72:251-65
26. Daudigeos-Dubus E, Le Dret L, Bawa O, Opolon P, Vievard A, Villa I, *et al.* Dual inhibition using cabozantinib overcomes HGF/MET signaling mediated resistance to pan-VEGFR inhibition in orthotopic and metastatic neuroblastoma tumors. Int J Oncol **2017**;50:203-11
27. Daudigeos-Dubus E, Le Dret L, Lanvers-Kaminsky C, Bawa O, Opolon P, Vievard A, *et al.* Regorafenib: Antitumor Activity upon Mono and Combination Therapy in Preclinical Pediatric Malignancy Models. PLoS One **2015**;10:e0142612
28. Calero R, Morchon E, Johnsen JI, Serrano R. Sunitinib suppress neuroblastoma growth through degradation of MYCN and inhibition of angiogenesis. PLoS One **2014**;9:e95628
29. Rossler J, Monnet Y, Farace F, Opolon P, Daudigeos-Dubus E, Bourredjem A, *et al.* The selective VEGFR1-3 inhibitor axitinib (AG-013736) shows antitumor activity in human neuroblastoma xenografts. Int J Cancer **2011**;128:2748-58
30. Cazes A, Lopez-Delisle L, Tsarovina K, Pierre-Eugene C, De Preter K, Peuchmaur M, *et al.* Activated Alk triggers prolonged neurogenesis and Ret upregulation providing a therapeutic target in ALK-mutated neuroblastoma. Oncotarget **2014**;5:2688-702
31. Chanthery YH, Gustafson WC, Itsara M, Persson A, Hackett CS, Grimmer M, *et al.* Paracrine signaling through MYCN enhances tumor-vascular interactions in neuroblastoma. Sci Transl Med **2012**;4:115ra3
32. Di Paolo D, Ambrogio C, Pastorino F, Brignole C, Martinengo C, Carosio R, *et al.* Selective therapeutic targeting of the anaplastic lymphoma kinase with liposomal

siRNA induces apoptosis and inhibits angiogenesis in neuroblastoma. Mol Ther **2011**;19:2201-12
33. Jamin Y, Glass L, Hallsworth A, George R, Koh DM, Pearson AD*, et al.* Intrinsic susceptibility MRI identifies tumors with ALKF1174L mutation in genetically-engineered murine models of high-risk neuroblastoma. PLoS One **2014**;9:e92886
34. Moreno L, Caron H, Geoerger B, Eggert A, Schleiermacher G, Brock P*, et al.* Accelerating drug development for neuroblastoma - New Drug Development Strategy: an Innovative Therapies for Children with Cancer, European Network for Cancer Research in Children and Adolescents and International Society of Paediatric Oncology Europe Neuroblastoma project. Expert Opin Drug Discov **2017**;12:801-11
35. Bid HK, Kerk S. BET bromodomain inhibitor (JQ1) and tumor angiogenesis. Oncoscience **2016**;3:316-7
36. Romain C, Paul P, Kim KW, Lee S, Qiao J, Chung DH. Targeting Aurora kinase-A downregulates cell proliferation and angiogenesis in neuroblastoma. J Pediatr Surg **2014**;49:159-65
37. Chen Z, Zhao Y, Yu Y, Pang JC, Woodfield SE, Tao L*, et al.* Small molecule inhibitor regorafenib inhibits RET signaling in neuroblastoma cells and effectively suppresses tumor growth in vivo. Oncotarget **2017**;8:104090-103
38. Kortlever RM, Sodir NM, Wilson CH, Burkhart DL, Pellegrinet L, Brown Swigart L*, et al.* Myc Cooperates with Ras by Programming Inflammation and Immune Suppression. Cell **2017**;171:1301-15 e14
39. Dejure FR, Eilers M. MYC and tumor metabolism: chicken and egg. EMBO J **2017**;36:3409-20
40. Berry T, Luther W, Bhatnagar N, Jamin Y, Poon E, Sanda T*, et al.* The ALK(F1174L) mutation potentiates the oncogenic activity of MYCN in neuroblastoma. Cancer Cell **2012**;22:117-30
41. Lopez-Delisle L, Pierre-Eugene C, Louis-Brennetot C, Surdez D, Raynal V, Baulande S*, et al.* Activated ALK signals through the ERK-ETV5-RET pathway to drive neuroblastoma oncogenesis. Oncogene **2018**
42. Huang D, Rutkowski JL, Brodeur GM, Chou PM, Kwiatkowski JL, Babbo A*, et al.* Schwann cell-conditioned medium inhibits angiogenesis. Cancer Res **2000**;60:5966-71
43. Chlenski A, Liu S, Crawford SE, Volpert OV, DeVries GH, Evangelista A*, et al.* SPARC is a key Schwannian-derived inhibitor controlling neuroblastoma tumor angiogenesis. Cancer Res **2002**;62:7357-63
44. Poliani PL, Mitola S, Ravanini M, Ferrari-Toninelli G, D'Ippolito C, Notarangelo LD*, et al.* CEACAM1/VEGF cross-talk during neuroblastic tumour differentiation. J Pathol **2007**;211:541-9
45. Gengenbacher N, Singhal M, Augustin HG. Preclinical mouse solid tumour models: status quo, challenges and perspectives. Nat Rev Cancer **2017**;17:751-65
46. Almeida GS, Panek R, Hallsworth A, Webber H, Papaevangelou E, Boult JK*, et al.* Pre-clinical imaging of transgenic mouse models of neuroblastoma using a dedicated 3-element solenoid coil on a clinical 3T platform. Br J Cancer **2017**;117:791-800
47. Verlhac S, Morel M, Bernaudin F, Bechet S, Jung C, Vasile M. Liver iron overload assessment by MRI R2* relaxometry in highly transfused pediatric patients: an agreement and reproducibility study. Diagn Interv Imaging **2015**;96:259-64
48. Peuchmaur M, d'Amore ES, Joshi VV, Hata J, Roald B, Dehner LP*, et al.* Revision of the International Neuroblastoma Pathology Classification: confirmation of favorable and unfavorable prognostic subsets in ganglioneuroblastoma, nodular. Cancer **2003**;98:2274-81

49. Toth GB, Varallyay CG, Horvath A, Bashir MR, Choyke PL, Daldrup-Link HE*, et al.* Current and potential imaging applications of ferumoxytol for magnetic resonance imaging. Kidney Int **2017**;92:47-66
50. Allen LM, Hasso AN, Handwerker J, Farid H. Sequence-specific MR imaging findings that are useful in dating ischemic stroke. Radiographics **2012**;32:1285-97; discussion 97-9

Figures

Figure 1

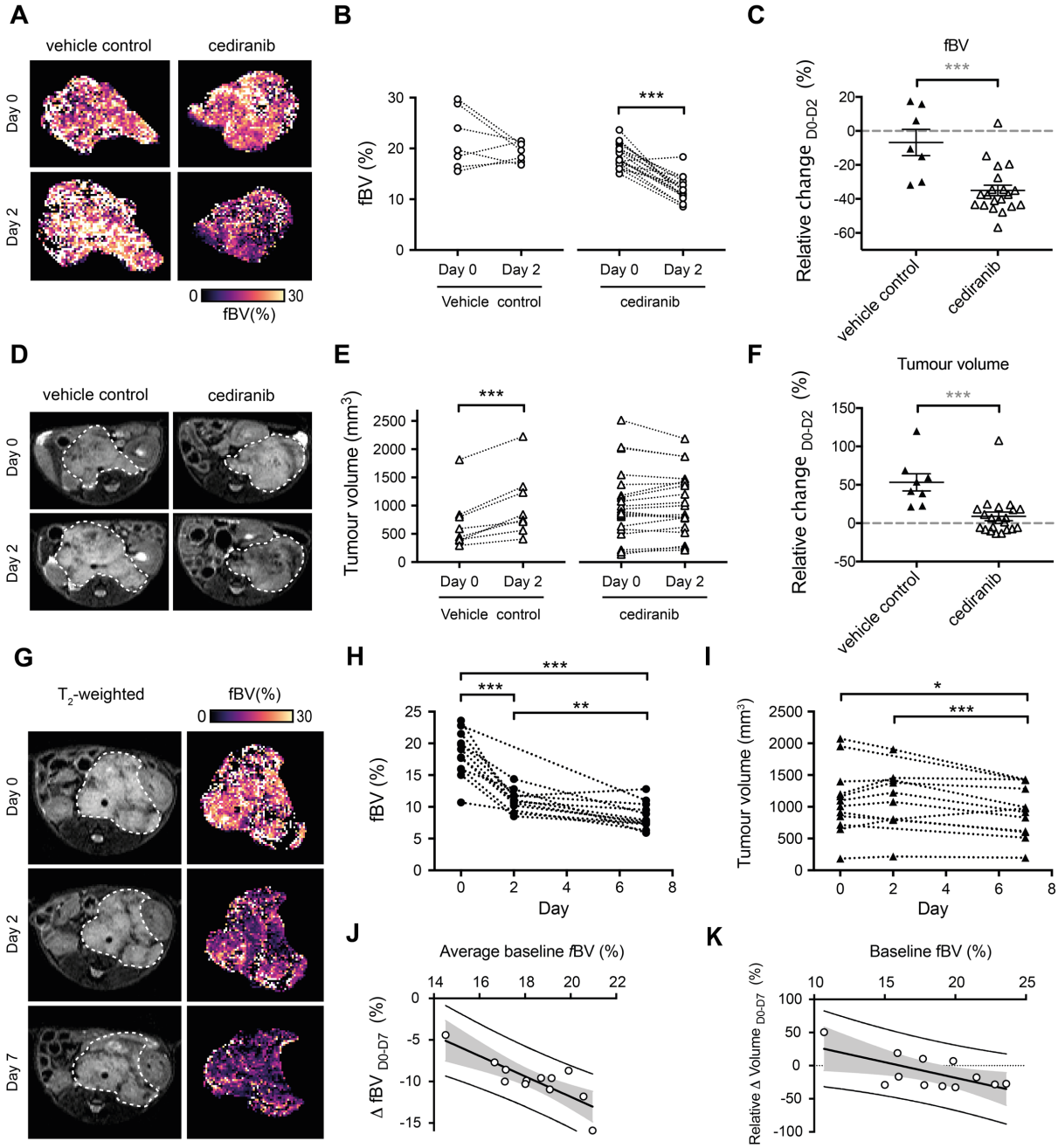

Fig. 1. Susceptibility-contrast MRI-derived fractional blood volume (*f*BV) predicts response to vascular endothelial growth factor receptor (panVEGFR) inhibitor cediranib in the Th-*MYCN* model of neuroblastoma. (**A**) Representative tumor parametric *f*BV maps in the Th-*MYCN* mice prior to (Day 0) and 24h (Day 2) after treatment with 6mg/kg cediranib or vehicle. Changes (**B**) and relative changes (**C**) in tumor median fBV prior to (Day 0) and 24h (Day 2) after treatment with 6mg/kg cediranib or vehicle. (**D)** Representative T_2-weighted anatomical MRI taken through the abdomen of tumor-bearing Th-*MYCN* mice prior to (Day 0) and 24h (Day 2) after treatment with 6mg/kg cediranib or vehicle. (**E**) Changes and (**F**) relative changes in tumor volume prior to (Day 0) and 24h (Day 2) after treatment with 6mg/kg cediranib or vehicle. Data are the individual median value for each tumor and the cohort mean ± 1 s.e.m. (***p<0.005, two-tailed paired Student's t-test; **p<0.01, ***p<0.005, two-tailed unpaired Student's t-test, 5% level of significance). (**G**) Representative T_2-weighted anatomical MRI and tumor fBV parametric map of a Th-*MYCN* mouse prior, 24h and 7 days after daily treatment with 6mg/kg cediranib. (**H**) Changes in tumor fBV and **(I)** tumor volume in Th-*MYCN* mice prior, 24h and 7 days after daily treatment with 6mg/kg cediranib. **(J)** Average tumor median *f*BV correlated with change in *f*BV over the 7 days of the trial (r= -0.83, p=0.0008). (**K)** Tumor median *f*BV correlated with change in tumor volume over the 7 days of the trial (r= -0.65, p=0.02).

Figure 2

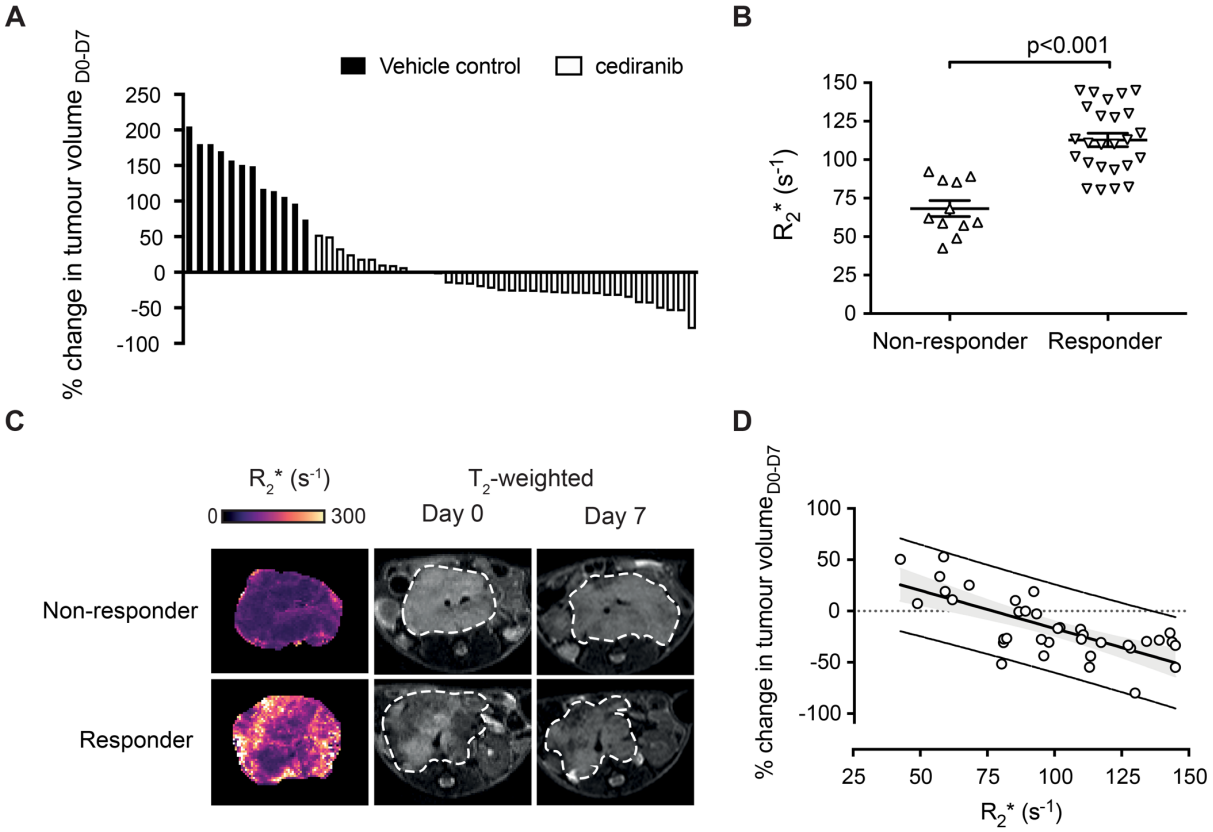
A
Vehicle control
cediranib
% change in tumour volume D0-D7
250
200
150
100
50
0
-50
-100
B
p<0.001
R_2^* (s^{-1})
150
125
100
75
50
25
0
Non-responder
Responder
C
R_2^* (s^{-1})
0
300
T_2-weighted
Day 0
Day 7
Non-responder
Responder
D
% change in tumour volume D0-D7
100
50
0
-50
-100
25
50
75
100
125
150
R_2^* (s^{-1})

Fig. 2. Intrinsic susceptibility MRI-derived transverse relaxation rate R_2* predicts response to vascular endothelial growth factor receptor (panVEGFR) inhibitor cediranib in the Th-*MYCN* model of neuroblastoma. (**A**) Waterfall plot documenting relative changes in tumor volume in the Th-*MYCN* mouse model of neuroblastoma following seven-day treatment with daily dose of 6mg/kg cediranib or vehicle ($\Delta Volume_{cediranib\_D0\text{-}D7}$= -16±5% vs $\Delta Volume_{vehicle\_D0\text{-}D7}$= 142±11%, $p<0.0001$, two-tailed unpaired Student's t-test with a 5% level of significance). (**B**) Baseline R_2* value (Day 0) of responsive and non-responsive tumors (Data are the individual median value for each tumor and the cohort mean ± 1 s.e.m., $p<0.0001$, two-tailed unpaired Student's t-test with a 5% level of significance). (**C**) Representative baseline native R_2* maps for responsive and progressive tumors in Th-*MYCN* transgenic mice (assessed by anatomical MRI) following daily treatment with 6mg/kg cediranib for 7 days. (**D**) Native tumor median R_2* (Day 0) correlated with relative change in tumor volume following daily treatment with 6mg/kg cediranib for 7 days ($r= -0.72$, $p<0.001$).

Figure 3

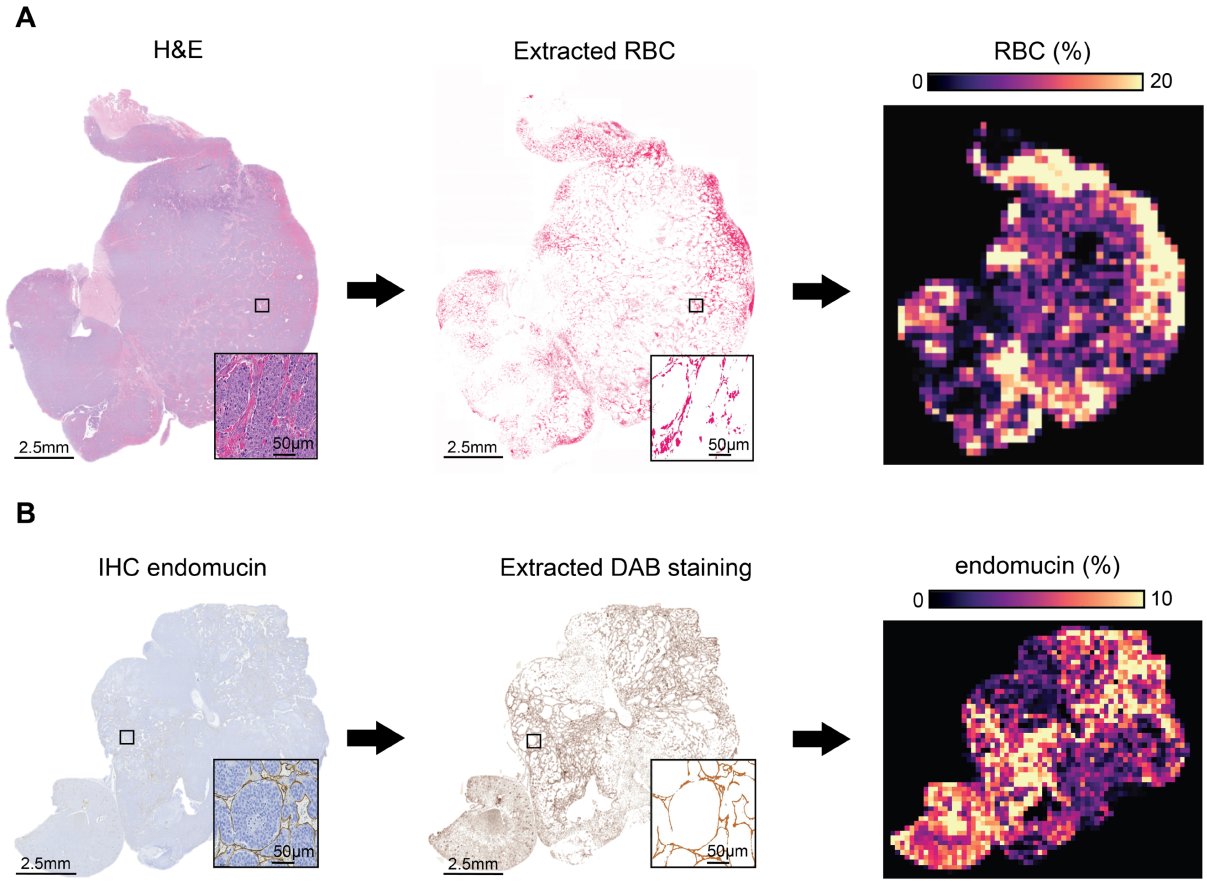
A
H&E
Extracted RBC
RBC (%)
0
20
2.5mm
50μm
2.5mm
50μm
B
IHC endomucin
Extracted DAB staining
endomucin (%)
0
10
2.5mm
50μm
2.5mm
50μm

Fig. 3. Pipeline for the generation of computed maps of red blood cells (RBC) and endomucin staining from histopathological images in Th-*MYCN* tumors. **(A)** RBC were automatically extracted from hematoxylin and eosin (H&E)-stained whole section slides with an accuracy of 99.74%. **(B)** Endomucin staining was extracted from chromogenic immunohistochemistry whole section slides with an accuracy of 97%. Note that the contrast of the whole slide extracted endomucin was enhanced, solely for printing visibility. Whole-section images were subsequently processed to match the MRI resolution, with the fraction of pixels occupied by red blood cells (**A**) and endomucin (**B**) within 518x518 pixels of the original images, representing a single pixel in the final maps.

Figure 4

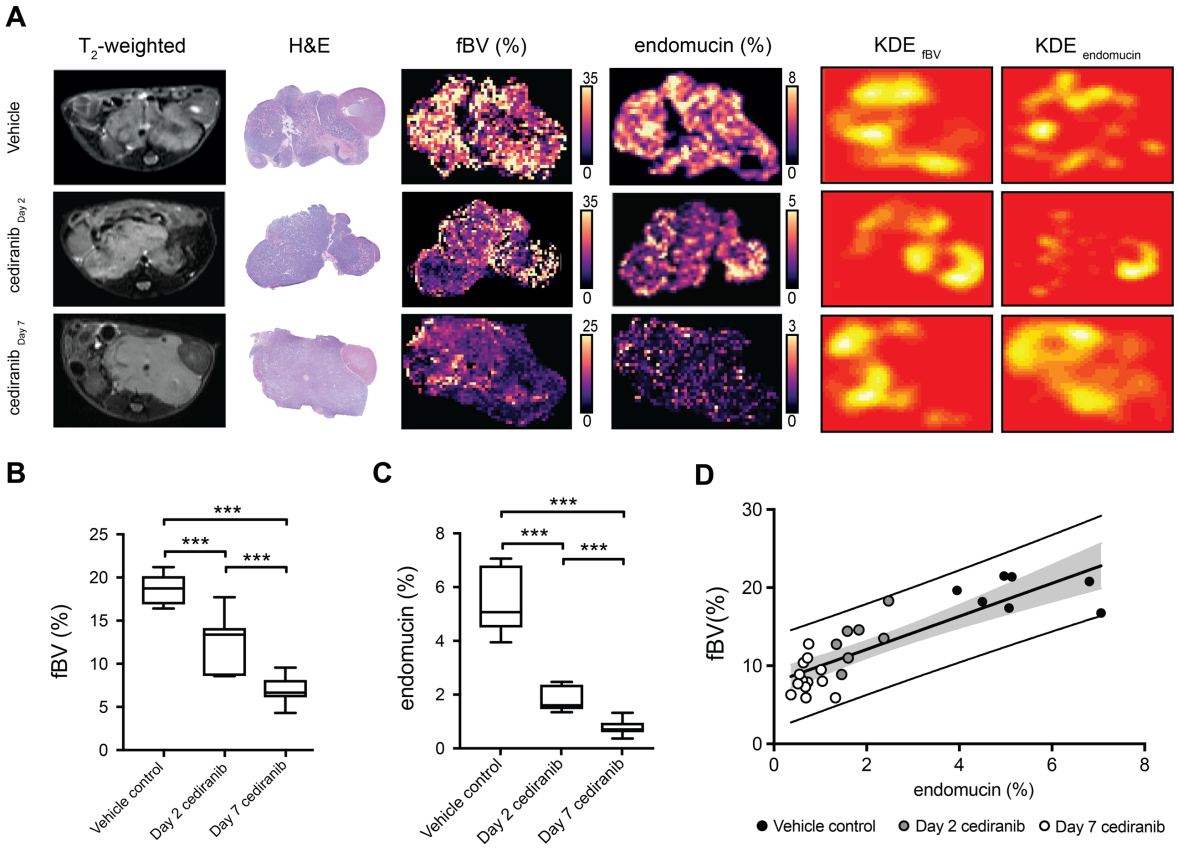
A
T2-weighted
H&E
fBV (%)
endomucin (%)
KDE fBV
KDE endomucin
Vehicle
cediranib Day 2
cediranib Day 7
35
0
8
0
35
0
5
0
25
0
3
0
B
fBV (%)
***
***
***
Vehicle control
Day 2 cediranib
Day 7 cediranib
C
endomucin (%)
***
***
***
Vehicle control
Day 2 cediranib
Day 7 cediranib
D
fBV(%)
endomucin (%)
Vehicle control
Day 2 cediranib
Day 7 cediranib

Fig. 4. Susceptibility-contrast MRI-derived fractional blood volume (*f*BV) correlates with endothelial cell marker endomucin fraction in tumors of the Th-*MYCN* model of neuroblastoma (**A**), Representative T_2-weighted anatomical MRI images and their corresponding H&E-stained histology, parametric *f*BV maps and computed areas of vascular endothelial cell marker endomucin staining, kernel density estimation (KDE) hotspot maps of high values (above the 85th percentile of each tumor sample) of *f*BV and endomucin fraction in the Th-*MYCN* model of neuroblastoma, 24 hours and 7 days after daily treatment with cediranib or vehicle (24 hours). (Note the different scale for *f*BV and endomucin maps across the groups to better capture the intratumoral heterogeneity). (**B)** Median tumor fBV and **(C)** median tumor endomucin fraction area in the Th-*MYCN* GEM model 24 hours and 7 days after treatment with cediranib or vehicle (***$p<0.001$, two-tailed unpaired Student's t-test). **(D)** Tumor median *f*BV correlated with endomucin fraction area ($r= 0.85$, $p<0.0001$).

Figure 5

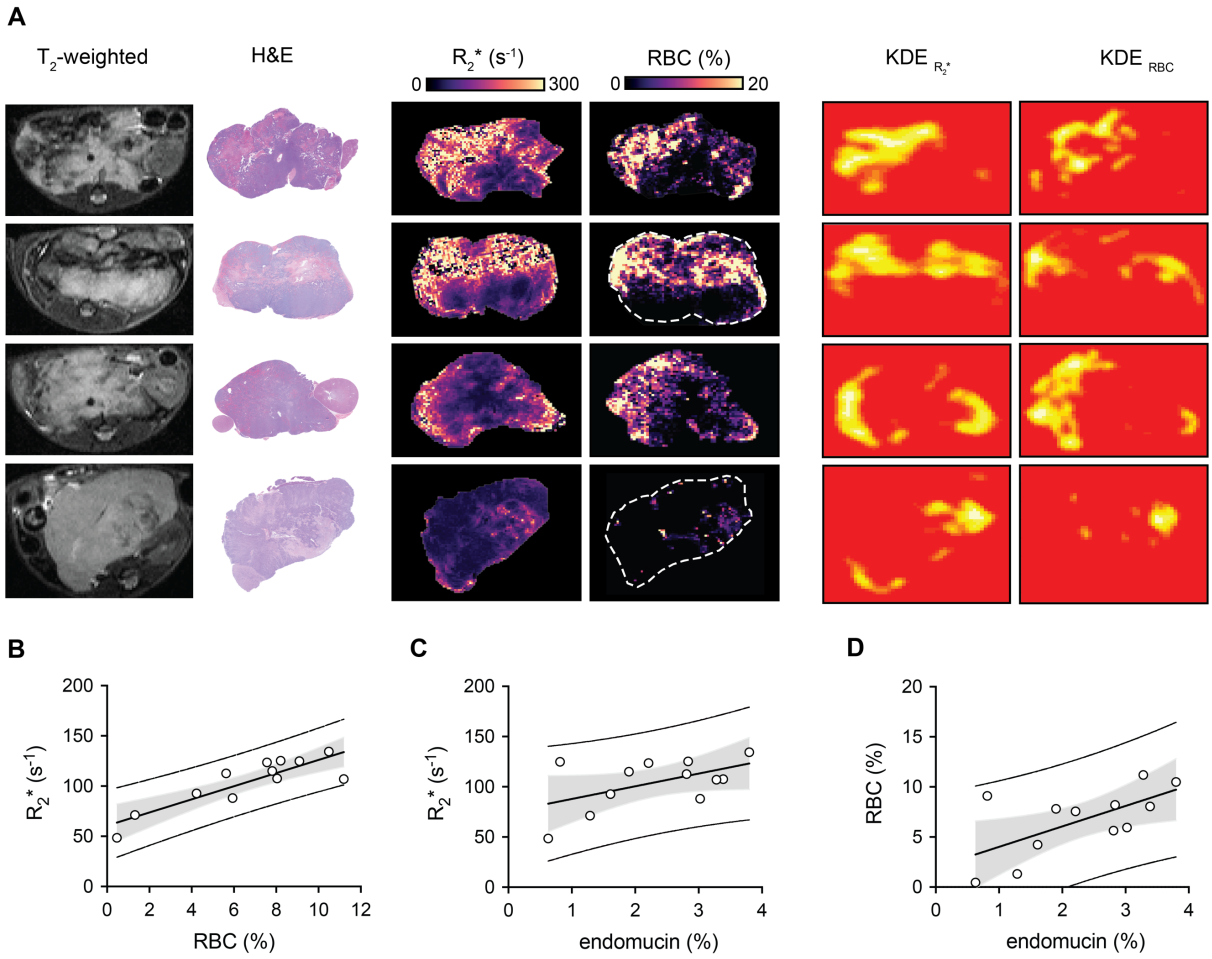
A
T2-weighted
H&E
R2* (s-1)
0
300
RBC (%)
0
20
KDE R2*
KDE RBC
B
R2* (s-1)
RBC (%)
C
R2* (s-1)
endomucin (%)
D
RBC (%)
endomucin (%)

Fig. 5. Intrinsic susceptibility MRI-derived transverse relaxation rate R_2* correlates with tumor red blood cells content. (**A**) Representative T_2-weighted MRI images and their corresponding H&E histology, maps of the transverse relaxation rate R_2* and computed area of red blood cells (RBC) detected from H&E stained images, kernel density estimation (KDE) hotspot maps of high values (above the 85th percentile of each tumor sample) of R_2* and RBC fraction in tumors arising in control Th-*MYCN* transgenic mouse. (**B**) Tumor median R_2* positively correlated with the mean value of RBC fraction detected from H&E stained tumors arising in the Th-*MYCN* transgenic mouse model, r= 0.87, p= 0.0003. R_2* values (**C**) and mean value of RBC fraction (**D**) also correlated with endomucin staining. (r= 0.53, p = 0.08 and r = 0.64, p = 0.02).

Figure 6

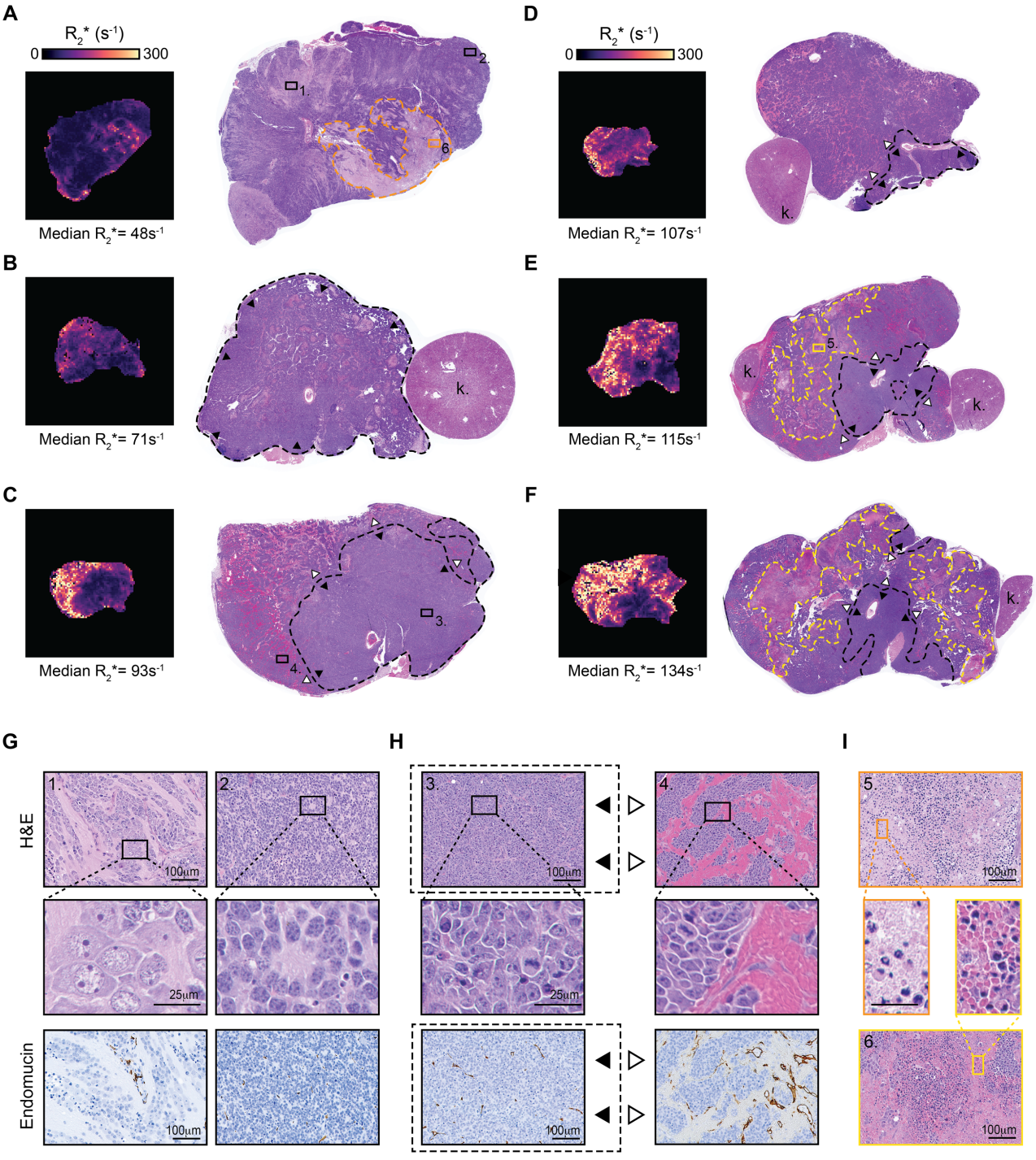
A
R2* (s-1)
0
300
Median R2*= 48s-1
1.
2.
6
D
R2* (s-1)
0
300
Median R2*= 107s-1
k.
B
Median R2*= 71s-1
k.
E
Median R2*= 115s-1
5.
k.
k.
C
Median R2*= 93s-1
3.
4.
F
Median R2*= 134s-1
k.
G
H
I
H&E
Endomucin
1.
2.
3.
4.
5.
6.
100µm
25µm

Fig. 6. Calibration of intrinsic susceptibility MRI-derived tumor R_2* phenotype with histopathological phenotype in the Th-*MYCN* genetically-engineered murine model of neuroblastoma. **(A-F)** show susceptibility-weighted MRI-derived maps of the tumor transverse relaxation R_2* and their corresponding hematoxylin and eosin (H&E)-stained whole-section slides (k., kidney), arranged by increasing median tumor R_2* value. Tumors with very low median value of R_2* (< $60s^{-1}$), (**A)** present with a differentiating phenotype characterized by **(G)** large areas of differentiating neuroblasts, with enlarged cytoplasm and more prominent nucleoli, surrounded by large amounts of neuropil (1.), alongside dense regions of undifferentiated neuroblast (2.). Note that hemorrhage is absent from these tumors and the vasculature is characterized by sparse capillaries-like blood vessels as revealed by immunohistochemistry staining for the vascular endothelial cells marker endomucin. For a median value of R_2* of ~70 s^{-1} and above, tumors present with dense area of poorly differentiated neuroblast presenting with numerous presence of mitotic features **(H)**, yet tumor median R_2* is determined by the increasing ratio of region with large area of hemorrhage and high vascular density (4., ---, ▷) over region with lower density of capillary like vessel (3., ---, ▶). Note that the extravasated red blood cells (RBCs) appear intact. Additionally, tumors with median R_2* over $110s^{-1}$ show vast area of cellular damage (necrosis) filled with intact and damaged RBCs **(I)** (---, 5). Necrotic area with low RBC content (---, 6) only present with small regional increase in R_2* (as seen in **(A)**).

Figure 7

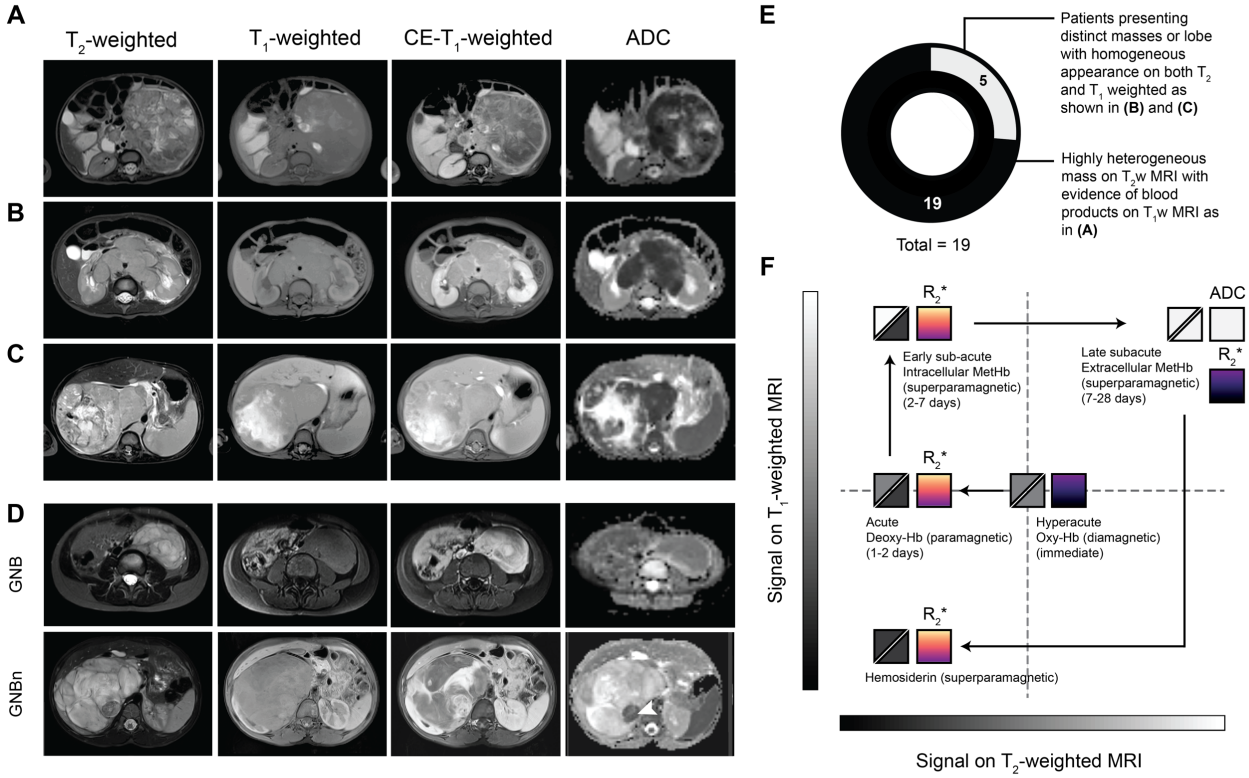
A
T2-weighted
T1-weighted
CE-T1-weighted
ADC
B
C
D
GNB
GNBn
E
Patients presenting distinct masses or lobe with homogeneous appearance on both T2 and T1 weighted as shown in (B) and (C)
5
19
Highly heterogeneous mass on T2w MRI with evidence of blood products on T1w MRI as in (A)
Total = 19
F
R2*
ADC
Early sub-acute Intracellular MetHb (superparamagnetic) (2-7 days)
Late subacute Extracellular MetHb (superparamagnetic) (7-28 days)
Acute Deoxy-Hb (paramagnetic) (1-2 days)
Hyperacute Oxy-Hb (diamagnetic) (immediate)
Hemosiderin (superparamagnetic)
Signal on T1-weighted MRI
Signal on T2-weighted MRI

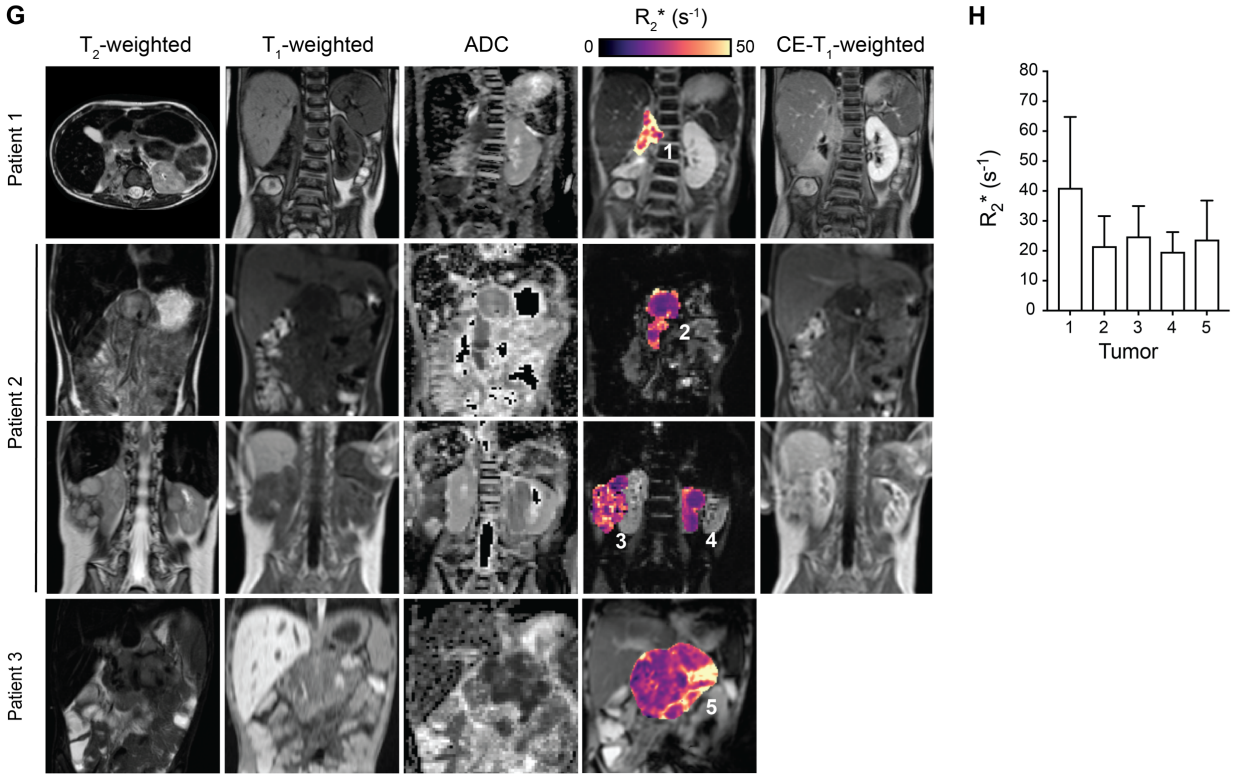
G
T2-weighted
T1-weighted
ADC
R2* (s-1)
0
50
CE-T1-weighted
Patient 1
Patient 2
Patient 3
1
2
3
4
5
H
R2* (s-1)
80
70
60
50
40
30
20
10
0
1
2
3
4
5
Tumor

Fig. 7. Hemorrhage in *MYCN*-amplified childhood neuroblastoma MRI and initial experience with SW-MRI in the neuroblastoma clinic. **(A-C)** show abdominal axial fat-suppressed STIR T_2-weighted-MRI images, fat-suppressed SPAIR T_1-weighted MRI images, before and after administration of gadolinium (Gd)-based contrast agent, and diffusion-weighted MRI-derived apparent diffusion coefficient (ADC) maps of children with neuroblastoma (NB) at the time of diagnosis. **(A)** *MYCN*-amplified high-risk neuroblastoma in a 10-month old boy, **(B)** a 2-year old boy, **(C)** a 8-month-old boy, **(D)** Comparison between a ganglioneuroblastoma (GNB) in a 4-year-old female patient and ganglioneuroblastoma nodular (GNB) in a 5-year-old male patient. Note the presence of the neuroblastic nodule in the GNBn easily identified on ADC maps (arrow head) **(E)** Proportion of patients with *MYCN*-amplified neuroblastoma (n=19) presenting with a MRI phenotype suggestive of the presence or absence of a hemorrhagic phenotype, based on the well-established knowledge of the appearance of ageing blood in hematoma on conventional MRI (50) as illustrated in **(F)**. **(G)** show abdominal T_2-weighted and T_1-weighted images (not fat-suppressed), ADC maps, intrinsic susceptibility MRI-derived transverse relaxation R_2* map of tumors, and post Gd contrast-enhanced T_1-weighted MRI images in children with refractory/relapsing neuroblastoma. (Patient 1: 7-year old male, Patient 2: 5-year old male, Patient 3: 6-year old female). **(H)** Tumor median R_2* values for each individual tumor shown in **(G)** (±SD). Note that R_2* values increased monotonically and approximatively linearly with magnetic field strength-dependent and as such clinical R_2* value at 1.5T are estimated to be four times lower that if they were measured at 7T (46).